

BAPGAN: GAN-BASED BONE AGE PROGRESSION OF FEMUR AND PHALANGE X-RAY IMAGES

Shinji Nakazawa¹, Changhee Han², Joe Hasei³, Ryuichi Nakahara⁴, Toshifumi Ozaki⁴

¹ LPIXEL Inc., Tokyo, Japan

² Saitama Prefectural University, Saitama, Japan

³ Okayama City General Medical Center, Okayama City Hospital, Okayama, Japan

⁴ Dept. of Orthopaedic Surgery, Grad. School of Medicine, Dentistry and Pharmaceutical Sciences, Okayama University, Okayama, Japan

ABSTRACT

Convolutional Neural Networks play a key role in bone age assessment for investigating endocrinology, genetic, and growth disorders under various modalities and body regions. However, no researcher has tackled bone age progression/regression despite its valuable potential applications: bone-related disease diagnosis, clinical knowledge acquisition, and museum education. Therefore, we propose Bone Age Progression Generative Adversarial Network (BAPGAN) to progress/regress both femur/phalange X-ray images while preserving identity and realism. We exhaustively confirm the BAPGAN’s clinical potential *via* Fréchet Inception Distance, Visual Turing Test by two expert orthopedists, and t-Distributed Stochastic Neighbor Embedding.

Index Terms— Generative Adversarial Networks, Medical Image Synthesis, Bone X-ray, Age Progression, Visual Turing Test

1. INTRODUCTION

Because skeletal maturity progresses through discrete stages, pediatric medicine has correlated children’s chronological age with bone age to investigate endocrinology, genetic, and growth disorders; but, time-consuming manual bone age assessment methods [1, 2] suffer from intra- and inter-observer variability. In this context, Convolutional Neural Networks have shown great promise in age assessment on various modalities and body regions, including hand/pelvic X-ray [3, 4], clavicle Computed Tomography [5], and hand Magnetic Resonance Imaging [6].

Along with the assessment, bone age progression/regression (i.e., predicting a given bone image’s future/past appearance) also matters because obtaining desired bone age images could lead to valuable applications: diagnosis (e.g., locating tumors around growth plates, such as osteosarcoma and aneurysmal bone cysts); clinical knowledge acquisition (e.g., how progression in epiphyseal width relates to epiphyseal fusion); museum education for children (e.g., height prediction). In Computer Vision, such face age progression using Generative Adversarial Networks (GANs)

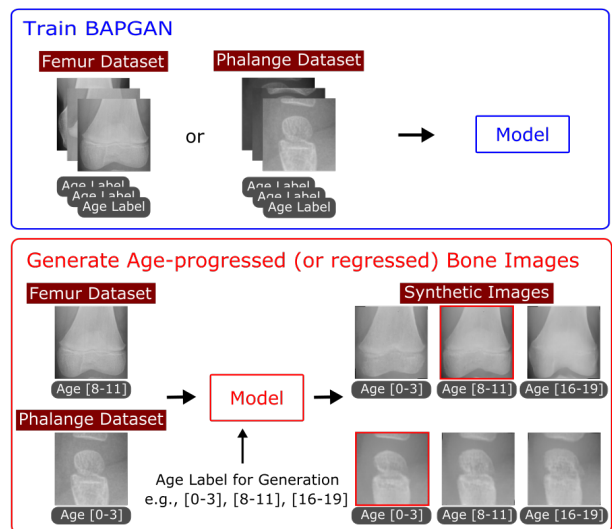


Figure 1: BAPGAN-based identity-preserved and realistic 128×128 X-ray image generation at desired bone age.

plays a key role in age-invariant verification/entertainment; Conditional Adversarial AutoEncoder (CAAE) is known for its age progression without paired samples [7]. However, no medical imaging researcher has tackled this despite the GANs’ growing clinical attention [8, 9]. Moreover, no bone age assessment method has analyzed multiple datasets [10].

We propose Bone Age Progression GAN (BAPGAN) to progress/regress both femur/phalange X-ray images while preserving identity and realism (Fig. 1). Since our task targeting ages 0–19 requires capturing short-term local subtle changes (especially around joints/growth plates) unlike the face age progression targeting all ages, we make these modifications to the CAAE: (i) an age discriminator; (ii) age label smoothing; (iii) Self-Attention (SA) modules. We exhaustively confirm its clinical potential *via* Fréchet Inception Distance (FID) [11], Visual Turing Test [12] by two expert orthopedists, and t-Distributed Stochastic Neighbor Embedding (t-SNE) [13].

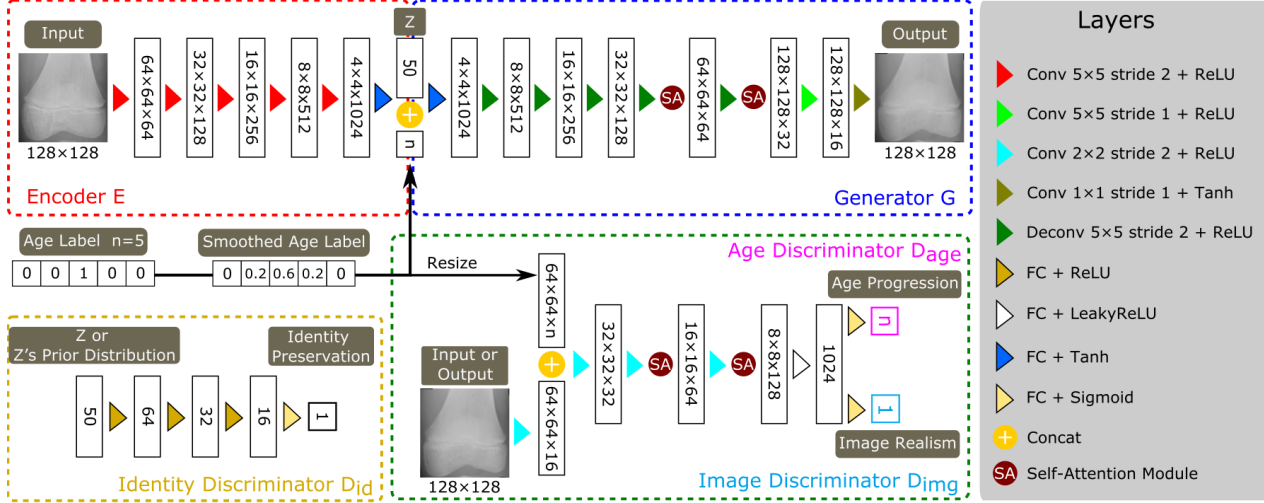


Figure 2: BAPGAN architecture for identity-preserved, realistic, and age-progressed 128×128 bone image generation: (a) the identity discriminator D_{id} aims to classify a latent variable z vs its prior distribution; (b) the image discriminator D_{img} learns to classify real vs synthetic bones; (c) the age discriminator D_{age} learns to categorize bone age.

Contributions. Our main contributions are as follows:

- **Multi-Dataset Bone Age Analysis:** This computational study firstly investigates how joint/growth plate appearances are associated with bone age on multiple datasets.
- **Bone Age Progression:** This first bone age progression approach shows that BAPGAN can generate identity-preserved/realistic X-ray images at desired bone age.
- **Clinical Potential:** This preliminary research qualitatively and quantitatively assesses BAPGAN-generated images for potential valuable applications: bone-related disease diagnosis, clinical knowledge acquisition, and museum education.

2. MATERIALS AND METHODS

2.1. Femur X-ray Dataset

We use a dataset of the lower extremity of femur X-ray images, cropped from healthy left leg X-ray images (image resolution: $1,793 \pm 975 \times 1,718 \pm 428$). The dataset was collected by the authors at Suiwakai Mizushima Central Hospital, Okayama, Japan, which is currently not publicly available due to ethical restrictions. The images are resized to 128×128 pixels after rotation correction. Subjects' age intervals are defined as: age [0-3]/[4-7]/[8-11]/[12-15]/[16-19] (42/47/56/130/42 images, respectively).

Similar to height increase, growth plates in children's femur stop growing and close near the end of puberty through discrete stages; similarly, surrounding bones gradually stop connecting to their joints. Thus, we use a 4-year equal interval classification scheme for bone age progression/regression. The dataset with 317 images is randomly split into: training/validation/test sets (223/32/62 images, respectively).

2.2. Phalange X-ray Dataset

This paper also uses a dataset of the middle phalange of index finger X-ray images, cropped from healthy left hand X-ray images (image resolution: $1,337 \pm 238 \times 1,680 \pm 300$). The dataset was extracted from RSNA Pediatric Bone Age Challenge [14]. The images are resized to 128×128 pixels after rotation correction. Subjects' age intervals are defined as: age [0-3]/[4-7]/[8-11]/[12-15]/[16-19] (137/1,309/2,514/2,912/293 images, respectively).

The phalange dataset is imbalanced towards age [4-15] as the challenge mainly predicts the age of middle childhood/early adolescence. The growth of children's phalange is smaller than that of children's femur on the images. The dataset with 7,165 images is randomly split into: training/validation/test sets (5,015/717/1,433 images, respectively).

2.3. Proposed Bone Age Progression Approach

2.3.1. BAPGAN-based Bone Age Progression

BAPGAN is a novel image-to-image GAN for bone age progression/regression (Fig. 2). It extends CAEE [7], which was originally conceived for face age progression/regression. The BAPGAN aims to capture short-term local subtle bone appearance changes between ages 0-19.

The CAEE, which is a GAN and AAE-combined end-to-end architecture, consists of four networks: an encoder E , a generator G , an identity discriminator D_{id} , and an image discriminator D_{img} . E encodes an input image x to a latent variable z to preserve the subject's identity. G generates a synthetic image x' given z and the subject's one-hot vector age label l . D_{id} aims to classify z vs its prior uniform distribution $p(z)$ for identity-preserved image generation while D_{img} learns to classify x vs x' for realistic/plausible image generation. To sum up, the CAEE (a version

without a total variation loss) adopts the following loss:

$$\begin{aligned} \mathcal{L}_{CAAE}(x, l) = & \min_{E, G} \max_{D_{id}, D_{img}} \lambda_1 \mathcal{L}(x, G(E(x), l)) \\ & + \mathbb{E}_{z^* \sim p(z)} [\log D_{id}(z^*)] \\ & + \mathbb{E}_{x \sim p_d(x)} [\log(1 - D_{id}(E(x)))] \\ & + \mathbb{E}_{x, l \sim p_d(x, l)} [\log D_{img}(x, l)] \\ & + \mathbb{E}_{x, l \sim p_d(x, l)} [\log(1 - D_{img}(G(E(x), l)))] \end{aligned} \quad (1)$$

where $p_d(x, l)$ denotes a training data distribution, z^* indicates z sampled from the prior, and \mathcal{L} is ℓ_2 norm. λ_1 balances smoothness and high resolution [7].

As shown in Fig. 2, our BAPGAN adopts the following modifications to improve realism and age progression:

Age Discriminator To explicitly represent aging effects, we introduce an age discriminator D_{age} and employ multi-task learning with D_{img} . The loss from classifying x into 6 age classes helps optimize D_{img} while the loss from classifying x' into 6 age classes helps optimize G as follows:

$$\begin{aligned} \mathcal{L}_{D_{age}}(x, l) = & \min_{E, G} \max_{D_{age}} \mathbb{E}_{x, l \sim p_d(x, l)} [-\log D_{age}(l|x)] \\ & + \mathbb{E}_{x, l \sim p_d(x, l)} [-\log D_{age}(l|G(E(x), l))] \end{aligned} \quad (2)$$

Age Label Smoothing To regularize ambiguous adjacent bone age representation, we smooth l with smoothing 0.2 (e.g., [0, 0, 1, 0, 0] to [0, 0.2, 0.6, 0.2, 0], [1, 0, 0, 0, 0] to [0.8, 0.2, 0, 0, 0]). l^{LS} denotes such a smoothed age label.

SA Modules To ignore noise and concentrate on bone age-relevant body parts by learning global and long-range dependencies, we apply SA modules after the designated convolutional/deconvolutional layers in $G/D_{img}/D_{age}$. Following the original paper [15], we also adopt spectral normalization [16] after each convolutional layer in $D_{id}/D_{img}/D_{age}$ and imbalanced learning rate for stable GAN training.

Finally, our BAPGAN loss becomes:

$$\mathcal{L}_{BAPGAN}(x, l^{LS}) = \mathcal{L}_{CAAE}(x, l^{LS}) + \lambda_2 \mathcal{L}_{D_{age}}(x, l^{LS}), \quad (3)$$

where λ_2 is a weight coefficient of $\mathcal{L}_{D_{age}}$.

BAPGAN Implementation Details We compare BAPGAN against CAAE, CAAE with only an age discriminator/age label smoothing, and CAAE with only SA modules (and stabilization techniques). Each GAN training lasts for 5.0×10^4 steps with a batch size of 32. With Adam optimizer ($\beta_1 = 0.5, \beta_2 = 0.999$), we use 1.0×10^{-4} learning rate for $E/G/D_{id}$ and 4.0×10^{-4} for D_{img}/D_{age} . The prior is a uniform distribution with 50 dimension. λ_1 and λ_2 are set to be 10000 and 100. As data augmentation, after random 5-degree rotation, we apply randomly-selected two color enhancing operations (i.e., a limited version of RandAugment [17]) from [auto-contrast, contrast, brightness, sharpness, posterize].

2.3.2. Clinical Validation Using Visual Turing Test

On both femur/phalange datasets, we evaluate the (i) realism of 128×128 synthetic images by CAAE and BAPGAN

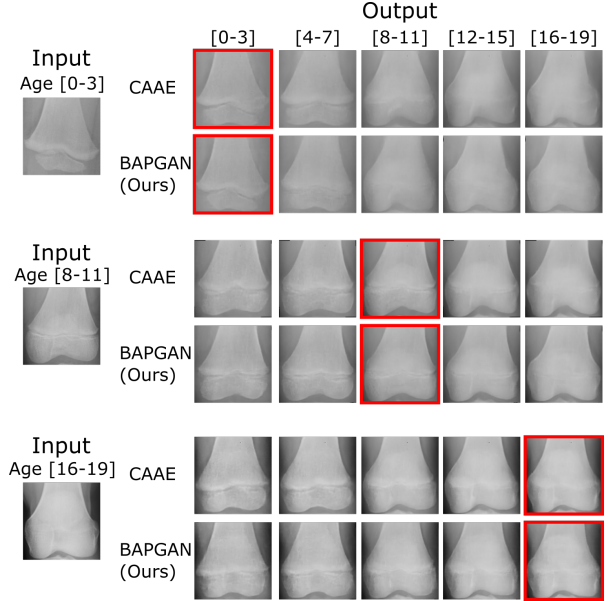


Figure 3: Example synthetic 128×128 Femur images. Red boxes denote age-invariant reconstruction results.

respectively against real images and its (ii) age progression/regression performance. First, we supply, in random order, to two orthopedists a random selection of 50 real and 50 synthetic images. Then, the orthopedists are asked to classify them as real/synthetic. Similarly, the orthopedists also have to select age-progressed images between 25 real vs 25 their 8-year CAAE/BAPGAN-progressed images. We perform the same for 8-year regressed ones. It should be noted that we use a relatively-long age interval (i.e., 8-year) because of the limited clinical data against the subtle appearance changes. The Visual Turing Test [12] can probe physicians' ability to identify clinical attributes in GAN-generated images [18].

2.3.3. Visualization Using t-SNE

T-SNE [13] visualizes inter-age distributions of real/synthetic 128×128 femur/phalange images, respectively, on a random selection of 210 real, 210 CAAE-generated, and 210 BAPGAN-generated images. We select 42 images per each age label (210 in total); 42 is the maximum available number of the femur real images for age [0-3].

T-SNE Implementation Details T-SNE training lasts for 500 steps with 50 perplexity. We normalize pixels to [0, 1].

3. RESULTS

3.1. BAPGAN-generated Femur/Phalange X-ray Images

Our BAPGAN progresses/regresses bone images more clearly than CAAE, especially around joints and growth plates (Figures 3 and 4). Moreover, as measured by FID (calculated between real images/their age-invariant reconstruction over the whole data distribution using Inception-v3 [19]), the BAPGAN can generate remarkably more realistic images

Table 2: Visual Turing Test results by two orthopedists for classifying 50 real (**R**) vs 50 synthetic (**S**) images by CAAE and BAPGAN respectively. Proximity to 50% of accuracy is superior (chance = 50%).

		Orthopedist	Accuracy	R as R	R as S	S as R	S as S
CAAE	Femur Dataset	A	67%	74%	26%	43%	57%
		B	74%	95%	5%	55%	45%
	Phalange Dataset	A	73%	83%	17%	41%	59%
		B	85%	83%	17%	12%	88%
BAPGAN	Femur Dataset	A	76%	90%	10%	43%	57%
		B	86%	97%	3%	29%	71%
	Phalange Dataset	A	66%	69%	31%	39%	61%
		B	66%	90%	10%	68%	32%

Table 3: Visual Turing Test results by orthopedists for selecting age-progressed images between 25 real vs 25 their 8-year CAAE/BAPGAN-progressed images. We perform the same for 8-year age-regressed ones. Proximity to 100% of accuracy is superior (chance = 50%).

		Orthopedist	Accuracy	Progression	Regression
CAAE	Femur Dataset	A	94%	100%	88%
		B	96%	100%	92%
	Phalange Dataset	A	48%	88%	8%
		B	54%	40%	68%
BAPGAN	Femur Dataset	A	100%	100%	100%
		B	96%	100%	92%
	Phalange Dataset	A	46%	60%	32%
		B	60%	72%	48%

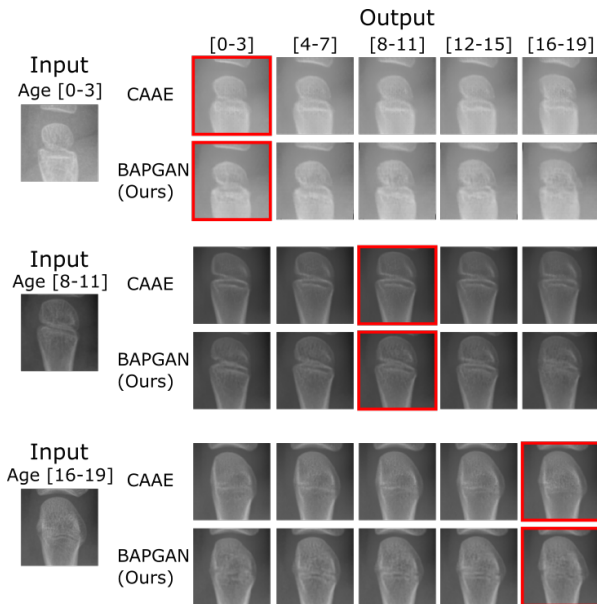


Figure 4: Example synthetic 128×128 Phalange images. Red boxes denote age-invariant reconstruction results.

(Table 1). A femur dataset shows comparatively high FID, especially with SA modules, due to its limited training data.

Table 1: FID for ablations of our proposed modifications to CAAE: D_{age} , LS, and SA represent an age discriminator, label smoothing, and SA modules, respectively.

		Model	D_{age}	LS	SA	FID
Femur Dataset		CAAE [7]	✗	✗	✗	125.82
		+ D_{age} , LS	✓	✓	✗	121.12
		+ SA	✗	✗	✓	148.13
		BAPGAN	✓	✓	✓	102.53
Phalange Dataset		CAAE [7]	✗	✗	✗	94.98
		+ D_{age} , LS	✓	✓	✗	76.25
		+ SA	✗	✗	✓	79.64
		BAPGAN	✓	✓	✓	43.73

3.2. Visual Turing Test Results

Two expert orthopedists fail to accurately recognize BAPGAN-generated images thanks to their realism and succeeds to recognize BAPGAN-progressed/regressed femur images (Tables 2 and 3). Meanwhile, recognizing phalange progression/regression is challenging due to its smaller growth on the images and training data imbalance.

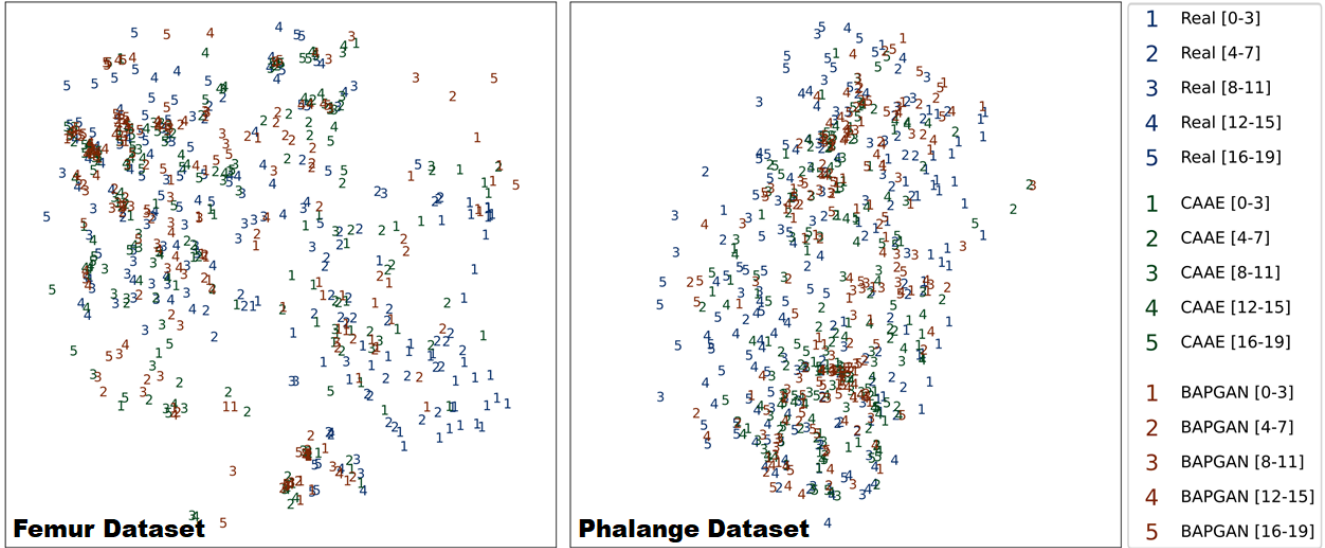


Figure 5: T-SNE plots with bone images: (a) real, (b) CAAE-generated, (c) BAPGAN-generated bones.

3.3. T-SNE Results

Real femur images for each age category are separately distributed except for age [12-15] and [16-19] since bone growth becomes slower until it ceases altogether (Figure 5). Meanwhile, distributions of real phalange images for age [4-19] highly overlap due to its smaller growth. BAPGAN-generated images have similar distributions to the real ones.

4. CONCLUSION

As confirmed by two expert orthopedists, our BAPGAN can translate both femur/phalange X-ray images into identity-preserved and realistic ones at desired bone age—those generated images could lead to valuable clinical applications (i.e., bone-related disease diagnosis, clinical knowledge acquisition, and museum education). This attributes to the BAPGAN’s good realism/age-progression performance capturing subtle bone appearance changes by combining an age discriminator/label smoothing with SA modules. Our BAPGAN points out new directions for research on time-series fine-grained image analysis in Computer Vision, such as remote sensing change prediction.

Our future work include considering sex differences since boys/girls have different timing of puberty (i.e., bone maturation); height growth is over when the boys/girls reach bone age 18/16, respectively [20]. Moreover, to synthesize and evaluate images with exact bone age, we plan to collect more training data and add class weights for handling class imbalance. Considering all distal/middle/proximal phalanges might be also helpful. Finally, We will investigate more GAN stabilization techniques, such as GAN losses [21], ℓ_1/ℓ_2 norm combination, and truncation trick [22].

5. REFERENCES

- [1] W. W. Greulich and S. I. Pyle, *Radiographic atlas of skeletal development of the hand and wrist*, Stanford university press, 1959.
- [2] J. M. Tanner, R. H. Whitehouse, N. Cameron, et al., *Assessment of skeletal maturity and prediction of adult height (TW2 method)*, Saunders London, 2001.
- [3] C. Spampinato, S. Palazzo, D. Giordano, et al., “Deep learning for automated skeletal bone age assessment in X-ray images,” *Med. Image Anal.*, vol. 36, pp. 41–51, 2017.
- [4] F. Fan, X. Dong, X. Wu, et al., “An evaluation of statistical models for age estimation and the assessment of the 18-year threshold using conventional pelvic radiographs,” *Forensic Sci. Int.*, vol. 314, pp. 110350, 2020.
- [5] S. Gassenmaier, J. F. Schaefer, K. Nikolaou, et al., “Forensic age estimation in living adolescents with CT imaging of the clavícula—impact of low-dose scanning on readers’ confidence,” *Eur. Radiol.*, pp. 1–8, 2020.
- [6] D. Štern, C. Payer, V. Lepetit, and M. Urschler, “Automated age estimation from hand MRI volumes using deep learning,” in *Proc. International Conference on Medical Image Computing and Computer-Assisted Intervention (MICCAI)*. Springer, 2016, pp. 194–202.
- [7] Z. Zhang, Y. Song, and H. Qi, “Age progression/regression by conditional adversarial autoencoder,” in *Proc. IEEE conference on Computer Vision and Pattern Recognition (CVPR)*, 2017, pp. 5810–5818.

- [8] B. Yu, L. Zhou, L. Wang, et al., “EA-GANs: edge-aware generative adversarial networks for cross-modality MR image synthesis,” *IEEE Trans. Med. Imaging*, vol. 38, no. 7, pp. 1750–1762, 2019.
- [9] C. Han, L. Rundo, R. Araki, et al., “Combining noise-to-image and image-to-image GANs: brain MR image augmentation for tumor detection,” *IEEE Access*, vol. 7, pp. 156966–156977, 2019.
- [10] A. L. Dallora, P. Anderberg, O. Kvist, et al., “Bone age assessment with various machine learning techniques: a systematic literature review and meta-analysis,” *PLoS one*, vol. 14, no. 7, pp. e0220242, 2019.
- [11] M. Heusel, H. Ramsauer, T. Unterthiner, et al., “GANs trained by a two time-scale update rule converge to a local nash equilibrium,” in *Advances in Neural Information Processing Systems (NIPS)*, 2017, pp. 6626–6637.
- [12] T. Salimans, I. Goodfellow, W. Zaremba, et al., “Improved techniques for training GANs,” in *Advances in Neural Information Processing Systems (NIPS)*, 2016, pp. 2234–2242.
- [13] L. van der Maaten and G. Hinton, “Visualizing data using t-SNE,” *J. Mach. Learn. Res.*, vol. 9, pp. 2579–2605, 2008.
- [14] S. S. Halabi, L. M. Prevedello, J. Kalpathy-Cramer, et al., “The RSNA pediatric bone age machine learning challenge,” *Radiology*, vol. 290, no. 2, pp. 498–503, 2019.
- [15] H. Zhang, I. Goodfellow, D. Metaxas, and A. Odena, “Self-attention generative adversarial networks,” in *Proc. International Conference on Machine Learning (ICML)*. PMLR, 2019, pp. 7354–7363.
- [16] T. Miyato, T. Kataoka, M. Koyama, and Y. Yoshida, “Spectral normalization for generative adversarial networks,” in *Proc. International Conference on Learning Representations (ICLR) arXiv:1802.05957*, 2018.
- [17] E. D. Cubuk, B. Zoph, J. Shlens, and Q. V. Le, “RandAugment: practical automated data augmentation with a reduced search space,” in *Proc. IEEE/CVF Conference on Computer Vision and Pattern Recognition (CVPR) Workshops*, 2020, pp. 702–703.
- [18] C. Han, H. Hayashi, L. Rundo, et al., “GAN-based synthetic brain MR image generation,” in *IEEE International Symposium on Biomedical Imaging (ISBI)*, 2018, pp. 734–738.
- [19] Christian Szegedy, Vincent Vanhoucke, Sergey Ioffe, et al., “Rethinking the inception architecture for computer vision,” in *Proc. IEEE conference on Computer Vision and Pattern Recognition (CVPR)*, 2016, pp. 2818–2826.
- [20] A. Parthasarathy, P. S. N. Menon, and M. K. C. Nair, *IAP textbook of pediatrics*, JP Medical Ltd, 2019.
- [21] X. Mao, Q. Li, H. Xie, et al., “Least squares generative adversarial networks,” in *Proc. IEEE International Conference on Computer Vision (ICCV)*, 2017, pp. 2794–2802.
- [22] A. Brock, J. Donahue, and K. Simonyan, “Large scale GAN training for high fidelity natural image synthesis,” in *Proc. International Conference on Learning Representations (ICLR) arXiv:1809.11096*, 2019.